Journal of Controlled Release 360 (2023) 304–315

Contents lists available at ScienceDirect

Journal of Controlled Release

journal homepage: www.elsevier.com/locate/jconrel

RGD-directed 24 nm micellar docetaxel enables elevated tumor-liver ratio, deep tumor penetration and potent suppression of solid tumors

Wencheng Yan [a], Beibei Guo [a,b], Zhe Wang [a], Jiangtao Yang [a], Zhiyuan Zhong [a,b,*], Fenghua Meng [a,*]

[a] Biomedical Polymers Laboratory, College of Chemistry, Chemical Engineering and Materials Science, and State Key Laboratory of Radiation Medicine and Protection, Soochow University, Suzhou 215123, PR China
[b] College of Pharmaceutical Sciences, Soochow University, Suzhou, 215123, PR China

ARTICLE INFO

Keywords:
Micelles
Docetaxel
Liver filtration
Tumor penetration
Targeted delivery

ABSTRACT

Nanomedicines while showing a great potential in improving the performance of chemotherapeutics like docetaxel (DTX) are distressed by a high liver deposition and poor tumor penetration, which might not only cause liver toxicity but also moderate therapeutic effect. Herein, we report that cRGD-directed 24 nm disulfide-crosslinked micellar docetaxel (cRGD-MDTX) presents low liver accumulation, high tumor uptake, and deep tumor penetration, leading to the potent suppression of different solid tumors. cRGD-MDTX was optimized with a cRGD density of 4% and DTX loading of 10 wt%. Interestingly, cRGD-MDTX enabled an extraordinary tumor-liver ratio of 2.8/1 with a DTX uptake of 8.3 %ID/g in $\alpha_v\beta_3$ over-expressing PC3 prostate tumor. The therapeutic studies demonstrated striking antitumor effects of cRGD-MDTX toward PC3 prostate tumor, prostate cancer patient-derived xenografts (PDX), orthotopic A549-Luc lung cancer and orthotopic SKOV3-Luc ovarian tumor models, in which tumor growth was effectually inhibited and 6–8 times better improvement of median survival time over free DTX was observed. This small disulfide-crosslinked micellar drug capable of relegating liver deposition opens a new avenue to nanomedicines for targeted therapy.

1. Introduction

Nanomedicines promise to elevate the performance of chemotherapeutics like docetaxel (DTX), paclitaxel (PTX), and doxorubicin (DOX), have shown tuned biodistribution, improved therapeutic efficacy and reduced toxicity compared to free drugs [1,2]. However, 30% - 99% of injected nanoparticles are typically sequestered in liver from blood circulation [3], causing hepatic toxicity and poor tumor deposition. The physiochemical properties of nanoparticles dictate their biodistribution and are responsible for discrepancy in hepatobiliary clearance [3–5]. The liver uptake of nanoparticles was reportedly dependent on their sizes [6,7] and surface properties [8].

Insufficient tumor deposition and penetration due to their relatively big size is another limiting factor for nanomedicines [9,10]. Small-sized nanomedicines while exhibiting better tumor penetration are confronted with reduced tumor retention [11,12]. To this end, sophisticated nanoparticles with charge-reversal (negative to positive) [13,14], size changeable [15,16], or active-targeting [17,18] properties were explored. It is of critical importance for nanomedicines to find strategies that are able to relegate liver deposition and increase tumor accumulation as well as penetration. Tumor neovasculature and several types of tumor cells are known to overexpress $\alpha_v\beta_3$ integrin [19,20], which renders it a highly interesting tool to enhance tumor retention as well as internalization of nanomedicines [21]. Cyclic RGD (cRGD) peptide has demonstrated particular specificity to $\alpha_v\beta_3$ integrin and clinical utility [22]. cRGD-ZW800–1 has entered phase 2 clinical trial for intraoperative NIR fluorescence imaging to assess tumor margin in cancer patients [23]. cRGD conjugation has shown to greatly enhance tumor accumulation and permeability of platinum(II)-complexed micelles [24]. Inadequate *in vivo* stability, drug leakage and fractional drug release at the tumor site are further problems for most of the reported nanomedicines [25]. The translation of nanomedicines has made very little progress partly because previous studies have mainly focused on only one or two of the many delivery issues. There are few reports on design of nanomedicines that display excellent stability, low liver deposition, high tumor uptake and penetration as well as fast release of

* Corresponding authors at: Biomedical Polymers Laboratory, College of Chemistry, Chemical Engineering and Materials Science, and State Key Laboratory of Radiation Medicine and Protection, Soochow University, Suzhou 215123, PR China.
E-mail addresses: zyzhong@suda.edu.cn (Z. Zhong), fhmeng@suda.edu.cn (F. Meng).

https://doi.org/10.1016/j.jconrel.2023.06.032
Received 4 March 2023; Received in revised form 14 June 2023; Accepted 22 June 2023
Available online 4 July 2023

drugs to the site of action.

Here, we find that integrin-targeting 24 nm robust biodegradable micellar DTX (cRGD-MDTX) based on dithiolane trimethylene carbonate (DTC) functionalized PEG-PLA is able to mitigate liver deposition, increase tumor accumulation, and penetrate deep into tumor, resulting in superior treatment of different solid tumor-bearing mice (Fig. 1A). We previously demonstrated that nanomedicines based on DTC-containing polymers hold a high stability and fast intracellular drug release [26,27], though they typically cause an excessive liver deposition because of large sizes. cRGD-MDTX was designed based on following considerations: (i) to minimize liver deposition, it should be small (average size <30 nm); (ii) to enhance tumor retention, it should be able to bind tumor vasculature and tumor cells; and (iii) to penetrate tumors and to be efficiently internalized by tumor cells, ligand density should be optimized. It is found that too strong affinity often retards tumor penetration and tumor cell uptake [28]. This represents an initial elaboration on robust and actively targeted nanotherapeutics that is capable of mitigating liver deposition, enhancing tumor uptake and penetration as well as triggering intracellular drug release.

2. Experimental section

2.1. Synthesis and characterization of PEG-P(LA-DTC)

PEG-P(LA-DTC) was synthesized by ring-opening polymerization of dithiolane trimethylene carbonate (DTC) and D,L-lactide (LA) using poly

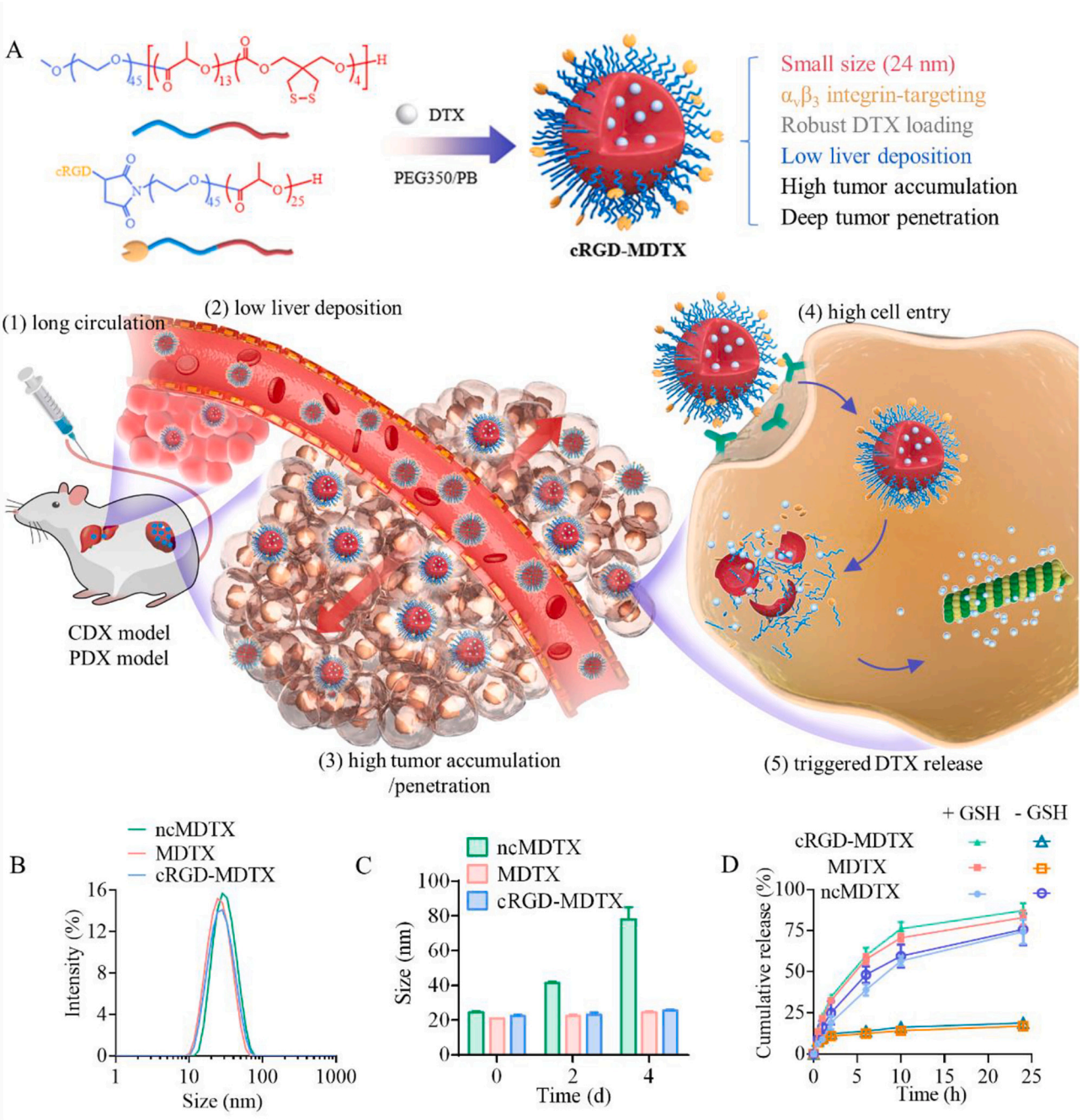

Fig. 1. Characteristics of cRGD-MDTX. (A) Illustration of formation and characteristics of cRGD-MDTX. (B) Size distribution profiles of ncMDTX, MDTX and cRGD-MDTX. (C) Size changes of different formulations at 37 °C over 4 days. (D) DTX release profiles at pH 7.4 with or without 10 mM GSH in 24 h (polymer conc. 1 mg/mL, $n = 3$).

(ethylene glycol) (PEG, M_n = 2.0 kg/mol) and 1,8-diazabicyclo[5.4.0] undec-7-ene (DBU) as an initiating system. In brief, in a nitrogen glove box, mPEG-OH (0.4 g, 200 μmol), DTC (0.14 g, 7.1 mmol) and LA (0.2 g, 13.9 mmol) were dissolved in dichloromethane (DCM) (10 mL) in a 25-mL Schlenk bottle, and then DBU (30 mg, 2 mmol) was added under stirring. After 3 h, one drop acetic acid was added to terminate the reaction , and the copolymer was recovered by precipitation twice in 20-fold cold diethylether, filtration and drying under vacuum. Yield: 76%. ^{1}H NMR (400 MHz, $CDCl_3$): PEG: δ 3.59 (-CH_2CH_2O-), 3.36 (CH_3O-); PLA: δ 5.14 (-COC*H*O-), 1.54 (CH_3-); PDTC: δ 4.19 (-OCH_2C-), 2.97 (-SCH_2C-). The molecular weight distribution (M_w/M_n) was determined by gel permeation chromatography.

2.2. Preparation and characterization of DTX-loaded micelles cRGD-MDTX

To prepare cRGD-MDTX with cRGD contents of 2%, 4% or 8%, cRGD-PEG-PLA, mPEG-P(LA-DTC) and DTX dissolved in PEG350 (at 50, 200 and 100 mg/mL, respectively) were mixed at molar ratio of 2/98, 4/96 or 8/92, and 50 μL of such mixture was injected into 950 μL of PB (pH 7.4, 10 mM, 60 °C) to obtain clear dispersions. The drug-loading content (DLC) was quantified *via* high performance liquid chromatography (HPLC). Cy5-labled micelles were prepared by mixing 0.5% (molar ratio) PEG-P(LA-DTC)-Cy5 to the above polymer mixture at 0.5/4/95.5. Non-targeted and non-crosslinked formulations, MDTX and ncMDTX, were prepared from mPEG-P(LA-DTC) and PEG-PLA, respectively. Empty micelles, cRGD-Ms, Ms and ncMs, were prepared in the same way but without DTX. The size, size distribution and stability in FBS were monitored by dynamic laser scattering (DLS).

2.3. Cellular uptake of cRGD-MDTX

To study *in vitro* cellular uptake, PC3, A549, SKOV3 or MCF-7 cells seeded in 6-well plates (3×10^5 /well) were incubated with Cy5 labeled cRGD-MDTX or MDTX for 4 h, and harvested, washed and resuspended for flow cytometry (FACS) analysis. For confocal laser scanning microscope (CLSM) studies, PC3 cells were seeded on coverslips in 24-well plates (3×10^5/well) overnight and then cultured with Cy5 labeled cRGD-MDTX and MDTX at 37 °C. After 4 h, the cells were washed, fixed with 4% paraformaldehyde, and stained with diamidino-phenyl-indole (DAPI) before CLSM observation. The inhibited uptake of Cy5 labeled cRGD-MDTX by free cRGD (1 mg/mL) pretreated PC3 cells was similarly conducted.

2.4. In vitro anti-tumor activity of cRGD-MDTX

In vitro cytotoxicity of MDTX and cRGD-MDTX was measured in $\alpha_v\beta_3$ overexpressing PC3, A549, SKOV3 cells and $\alpha_v\beta_3$ low expressing MCF-7 cells using 3-(4,5-dimethylthiazol-2-yl)-2,5-diphenyltetrazolium bromide (MTT) assays. Typically, the cells in 96-well plates (2×10^3/well) were added with 20 μL of cRGD-MDTX, MDTX or free DTX (DTX conc: 0.001–10 μg/mL). After 4 h, the cells were cultured with fresh medium for 44 h. MTT assays were then conducted according to the protocol. The relative cell viability was determined by comparing the absorbance at 570 nm with control cells treated with only PBS (n = 6) and half-maximal inhibitory concentration (IC_{50}) was calculated employing Prism 7 four-parameter logistic equation.

2.5. Cell apoptosis and microtubule stabilization of cRGD-MDTX

For apoptosis study, PC3 cells in 6-well plates (5×10^4 cells/well) were incubated with cRGD-MDTX, MDTX, free DTX (DTX conc: 30 ng/mL) for 4 h, and subsequently incubated with fresh medium for 44 h. Cells were then detached using EDTA-free pancreatin and stained with 10 μL PI and 5 μL Annexin V-Alexa Fluor 647 for 15 min before immediate flow cytometry measurements.

To visualize the microtubule polymerization, PC3 cells (3×10^5 /well) on coverslips were treated with cRGD-MDTX or MDTX (DTX conc: 2 μg/mL) for 4 h and cultured in fresh medium for 44 h. Then the cells were fixed for 15 min, blocked by 0.1% triton and 5% goat serum for 1 h, and stained with α-tubulin antibody at 4 °C overnight. The cells were sequentially stained by Alexa-680 labeled anti-rat IgG secondary antibody for 1 h and DAPI for 5 min. The immunofluorescence images of PC3 cells were attained by CLSM.

2.6. Animal models

All animal procedures were performed in accordance with the Guidelines for Care and Use of Laboratory Animals of Soochow University (P.R. China) and approved by the Animal Ethics Committee of Soochow University. To establish mouse model bearing subcutaneous PC3 xenografts, PC3 cells (1×10^7 cells/mouse, 100 μL) were subcutaneously injected into the right flank of BALB/c nude mice. For prostate cancer patient derived xenograft (PDX) model, prostate cancer patient tumor tissues were collected with consent of the patient, which were approved by the ethics committee of the First Affiliated Hospital of Soochow University (Suzhou, P.R. China) in accordance with the Declaration of Helsinki protocol. PDX model was set up by implanting patient tumor bulk (50–100 mg) subcutaneously to the right flank of NOD/SICD mice. At tumor volume of about 500 mm^3, PDX tumors were taken and cut into small pieces that were implanted (*ca.* 50 mm^3) into right flank of NOD/SICD mice.

Orthotopic A549 xenograft was established by injecting 50 μL A549-Luc cells (1×10^6 cells/mouse) directly to the left lung lobe. The tumor bioluminescence imaging was monitored using an IVIS imaging system. Orthotopic SKOV3 xenograft was built by injecting 10 μL SKOV3-Luc cells (1×10^5 cells/mouse) to the right ovary that was exposed by surgery. After sealing the wound, the tumor growth was monitored using IVIS *in vivo* imaging system.

2.7. Pharmacokinetics and biodistribution studies

To investigate the pharmacokinetics of micellar DTX in healthy BALB/c mice, 200 μL cRGD-MDTX, MDTX, ncMDTX or free DTX were injected at DTX dose of 7.5 mg/kg (n = 3) *via* tail veins. At prescribed time points blood samples (*ca.* 70 μL) were withdrawn from the retro-orbital sinus, and 20 μL plasma was collected and added into 500 μL methanol/acetonitrile (*v*/v, 1/1) overnight. After centrifugation, the supernatants were evaporated, and 100 μL acetonitrile was added to dissolve DTX in the residues. After filtration, DTX was quantified by HPLC calculated from a standard curve acquired from the mixture of 20 μL plasma and DTX of known concentrations using the same method, and plotted against time to analyze elimination half-life ($t_{1/2,\beta}$) using PK Solver.

To investigate the biodistribution, Cy5-labeled cRGD-MDTX and MDTX were *i.v.* administered into the mice bearing subcutaneous PC3 xenografts (DTX dose: 7.5 mg/kg, 0.2 μg Cy5/mouse, n = 3). The mice were scanned to track Cy5 signal at prescribed time points by IVIS. After 24 h, tumors and major organs were collected, weighed, and imaged using IVIS system. Subsequently, tumors and organs were homogenized in 1 mL methanol, and stored at r.t. for 24 h to extract DTX. After centrifugation the supernatants were evaporated, and 0.1 mL acetonitrile was added. DTX content was quantified using HPLC and shown as injected dose per gram of tissue (% ID/g).

To investigate the distribution of micellar DTX inside tumor tissues, at 24 h post injection of Cy5-labeled cRGD-MDTX, the tumors were sliced, treated with DAPI (staining nuclei), primary rat antibody CD31 and secondary Alexa Fluor 488-conjugated anti-rat IgG (staining blood vessels) in that order. The peripheral and central regions of tumor slices were imaged using CLSM.

2.8. Treatment of cRGD-MDTX in mice bearing prostate CDX and PDX models

At PC3 tumor volume of about 100 mm^3, the mice were randomly divided into seven groups (day 0): cRGD-MDTX with cRGD density of 2%, 4% or 8%, MDTX, ncMDTX, free DTX (DTX dose: 7.5 mg/kg) and PBS ($n = 5$). DTX formulations were *i.v.* injected on day 0, 3, 6, and 9. Body weight and tumor volume ($V = W^2 \times L/2$, where W and L are width and length, respectively) of the mice were recorded every two days and normalized to the initial values on day 0. On day 14 the mice were sacrificed, blood was sampled for the detection of calcium ion and phosphate concentrations using assay kits, and tumors were weighed for calculating tumor inhibition rate (%) relative to PBS group. The major organs and tumors were fixed with 4% paraformaldehyde, and stained with terminal deoxynucleotidyl transferase-mediated nick end labeling (TUNEL) and imaged using CLSM.

At PDX tumor volume of *ca.* 100 mm^3, the mice were randomly assigned into five groups (day 0): cRGD-MDTX, MDTX, ncMDTX, free DTX (DTX dose: 7.5 mg/kg) and PBS ($n = 5$). DTX formulations were *i.v.* administrated into the PDX mice on day 0, 3, 6, and 9. Body weight and tumor volume were recorded every two days.

2.9. Therapeutic activity of cRGD-MDTX toward mice bearing orthotopic solid tumor models

For the mice bearing orthotopic A549-Luc tumors, when lung bioluminescence reached *ca.* 1×10^7 p/s/cm^2/sr (day −1), the mice were *i.v.* administered with cRGD-MDTX, MDTX, free DTX (DTX dose: 7.5 mg/kg) or PBS on day 0, 3, 6, 9 and 12 ($n = 5$). The mice were weighed every two days, and scanned on day −1, 5, 11, 17 and 32 using IVIS imaging system after injection luciferin potassium salt (75 mg/kg). Body weight and bioluminescence were given relative to the values of day −1. The survival rates of the mice were monitored, and the mice with body weight loss over 15% were also consider dead.

At ovarian bioluminescence of SKOV3-Luc tumor-bearing nude mice of 1×10^6 p/s/cm^2/sr (day −1), the mice were *i.v.* administered with cRGD-MDTX, MDTX, free DTX (DTX dose: 7.5 mg/kg) or PBS ($n = 5$) on day 0, 3, 6 and 9. Body weight, bioluminescence and survival rates of the mice were tracked similarly as above.

2.10. Statistical analysis

Data were expressed as mean ± s.d. Significant difference among groups was judged by one-way ANOVA with Tukey multiple comparison tests. Survival curves were analyzed by log-rank comparison test employing Prism 7 software. $^*p < 0.05$ was significant, and $^{**}p < 0.01$ and $^{***}p < 0.001$ were highly significant.

3. Results and discussion

3.1. Synthesis of PEG-P(LA-DTC) and cRGD-PEG-PLA

Aiming at developing an integrin-targeting, ultra-small robust biodegradable micellar DTX (cRGD-MDTX), we synthesized DTC-functionalized PEG-PLA, PEG-P(LA-DTC) by ring-opening copolymerization of LA and DTC using mPEG-OH and DBU as an initiating system. ^{1}H NMR spectrum illustrated besides signals attributable to PEG (δ 3.60, 3.36) and LA moieties (δ 5.14, 1.54), also resonances assignable to DTC (δ 4.19, 2.97) (Fig. S1A). The degree of polymerization of DTC and LA was determined by comparing the integrals of DTC at δ 4.19 and LA at δ 5.14 to PEG methylene at δ 3.60, respectively. The results showed that PEG-P(LA-DTC) was acquired with a controllable M_n of 2.0-(1.0–0.7) kg/mol and a unimodal distribution (M_w/M_n of 1.14) (Fig. S2). cRGD-PEG-PLA with an M_n of 2.0–2.0 kg/mol was synthesized similarly *via* ring-opening polymerization of LA with maleimide-functionalized PEG (Mal-PEG, $M_n = 2$ kg/mol), followed by Michael addition with cRGDfC. ^{1}H NMR spectra validated that the peak at δ 6.70 assignable to Mal disappeared and the characteristic peak of cRGD appeared at δ 7.13–7.27 (Fig. S1B, C), indicating successful conjugation. BCA assay revealed a cRGD functionality of *ca.* 98%.

3.2. Fabrication of cRGD-MDTX

cRGD-MDTX was fabricated by injecting a PEG350 solution of DTX, cRGD-PEG-PLA and PEG-P(LA-DTC) mixture into an aqueous solution. cRGD-MDTX with varying DTX loading (5–15 wt%) and cRGD contents (2%, 4% or 8%) could be facilely obtained with small and uniform hydrodynamic diameter (22 to 25 nm, PDI = 0.05–0.13, Fig. 1A) and weakly negative surface charge (−3.47 ~ −0.43 mV) (Table 1). The empty micelles, cRGD-Ms, had a similar size (Table S1). Static laser scattering (SLS) measurement of cRGD-Ms illustrated a hydrodynamic radius (R_h) of *ca.* 10.5 nm and $R_h/R_g = 0.759$ (Fig. S3A), pointing to a core-shell structure [29]. cRGD-Ms and Ms did not show critical micelle concentration (CMC) at >0.1 μg/mL while ncMs made of PEG-PLA displayed a CMC of *ca.* 9.4 μg/mL (Fig. S3B), confirming spontaneous disulfide-core-crosslinking in cRGD-Ms and Ms. as previously reported for DTC-containing polymersomes and micelles [26,30]. Consequently, cRGD-MDTX and MDTX demonstrated markedly improved stability compared with non-crosslinked ncMDTX (Fig. 1B). The clinical formulation, Nanoxel-PM™, was indicated to be used within 4 h after redissolution to prevent precipitation [31]. Nanodrugs maintaining small size *in vivo* are vital to penetrate deep into tumors [32,33]. cRGD-MDTX and MDTX quickly released 80% DTX with 10 mM glutathione (GSH) in 24 h, while merely 15% DTX was leaked under a non-reductive condition (Fig. 1C). In comparison, fast DTX release from ncMDTX was discerned either with or without GSH.

3.3. Cellular uptake and inhibitory effect of cRGD-MDTX toward PC3 cells

cRGD is reported to have targetability to $\alpha_v\beta_3$ integrins that over-express in many tumors and neovasculature [19,20,34,35]. Prostate cancer PC3 cells over-expressing $\alpha_v\beta_3$ [36,37] (Fig. S4) were used to evaluate the targetability of cRGD-MDTX. The internalization of Cy5-labeled cRGD-MDTX (cRGD content of 2%–8%) by the cells was assessed using FACS. The results showed that 4% cRGD-MDTX had the best uptake, which was 2.5-fold that of MDTX (Fig. 2A). CLSM confirmed significantly higher internalization of Cy5-labeled 4% cRGD-MDTX than Cy5-labeled MDTX in PC3 cells (Fig. 2B). The pretreatment of PC3 cells with free cRGD peptide reduced cell uptake, verifying the targeting effect cRGD-MDTX. 4% cRGD-MDTX was used in later studies if not otherwise stated. This result emphasizes the importance for nanomedicines to be equipped with a ligand and optimal density, as is reported previously [38]. The observed best targetability for 4% cRGD-MDTX is likely a balanced result from its steric hindrance, affinity, and cell receptor binding. It has been found that a high ligand density might reduce the total cellular uptake due to over-consumption of surface

Table 1
Characterizations of cRGD-MDTX and MDTX (n = 3).

Micelles	DLC (wt%)	Size [a] (nm)	PDI [a]	Zeta [b] (mV)
MDTX	5	22 ± 1	0.08 ± 0.01	−0.43 ± 0.09
	10	22 ± 1	0.05 ± 0.02	−0.77 ± 0.08
	15	25 ± 2	0.13 ± 0.02	−2.8 ± 0.09
4% cRGD-MDTX	5	24 ± 2	0.12 ± 0.02	−3.19 ± 0.02
	10	24 ± 1	0.05 ± 0.01	−2.70 ± 0.06
	15	25 ± 2	0.13 ± 0.03	−3.47 ± 0.09
2% cRGD-MDTX	10	23 ± 1	0.10 ± 0.01	−0.82 ± 0.02
8% cRGD-MDTX	10	25 ± 2	0.09 ± 0.02	−2.37 ± 0.05
ncMDTX	10	25 ± 1	0.07 ± 0.02	−1.37 ± 0.02

[a] Determined by DLS in PB (pH 7.4, 5 mM).
[b] Determined by an electrophoresis in PB (pH 7.4, 5 mM).

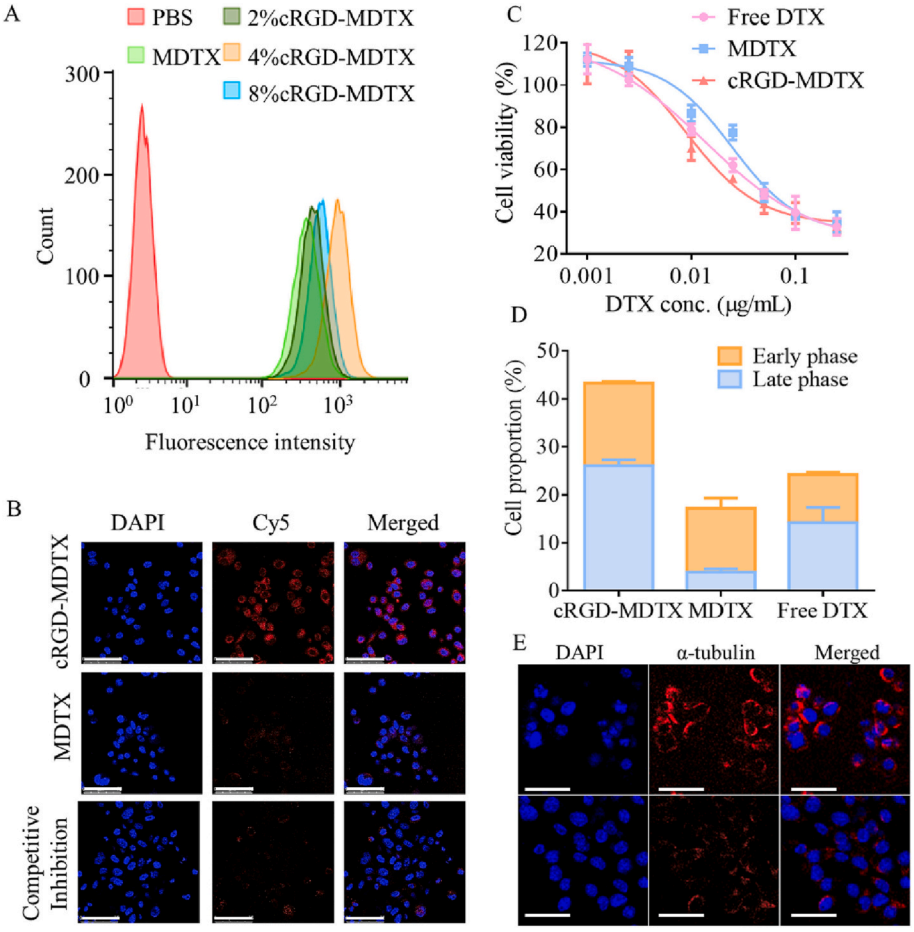

Fig. 2. Cell uptake and antitumor activity of cRGD-MDTX and MDTX in PC3 cells. (A) Flow cytometric analysis of PC3 cells at 4 h incubation with Cy5-labeled MDTX or cRGD-MDTX with various densities of cRGD. (B) CLSM images of PC3 cells at 4 h incubation with Cy5-labeled MDTX or cRGD-MDTX (free cRGD pretreated PC3 cells as control). Scale bar: 75 μm. (C) Antitumor activity and (D) apoptotic activity of cRGD-MDTX and MDTX toward PC3 cells. (E) Intracellular microtubule organization in PC3 cells (DTX: 0.3 μg/mL). For C-E, the cells were co-cultured 4 h with DTX formulations and 44 h with drug-free medium. Scale bar: 50 μm.

receptors [39], and too strong affinity does not enhance but retards tumor penetration [28]. The optimal ligand density also depends on particle size, wherein smaller nanoparticles tend to have lower optimal density [26,30]. A549 and SKOV3 cells were also found to overexpress $\alpha_v\beta_3$ (Fig. S4), for which cRGD-MDTX again demonstrated greatly higher cellular uptake than MDTX (Fig. S5A, B).

MTT assays unveiled that PC3 cells were very sensitive to DTX formulations, in which cRGD-MDTX had the best inhibitory effect with an IC_{50} of 29 ng/mL, *ca.* 2.0-fold lower than that of MDTX (Fig. 2C). The empty micelles, cRGD-Ms and Ms, did not show cytotoxic effect at high concentration up to 1.0 mg/mL (Fig. S5C), signifying an excellent biocompatibility. cRGD-MDTX also demonstrated considerably higher inhibitory effect than MDTX in A549 and SKOV3 cells (Fig. S5D, E). In contrast, similar IC_{50} was observed for cRGD-MDTX and MDTX in MCF-7 cells with low $\alpha_v\beta_3$ expression (Fig. S5F). The apoptosis assays exhibited that cRGD-MDTX induced significantly higher apoptosis of PC3 cells than MDTX and free DTX (Fig. 2D). CLSM images showed obvious aggregation of microtubules (α-tubulin) surrounding the nuclei of PC3 cells after treating with cRGD-MDTX (Fig. 2E), pointing to a strong inhibitive effect of microtubule depolymerization [40].

3.4. Pharmacokinetics and biodistribution of cRGD-MDTX

The pharmacokinetic studies in mice showed fast clearance of free DTX with an $t_{1/2,\beta}$ of 0.4 h (Fig. 3A). cRGD-MDTX and MDTX illustrated prolonged circulation time with $t_{1/2,\beta}$ of 4.9 and 5.0 h, respectively, which were about two times longer than ncMDTX and clinical DTX formulations, Nanoxel-PM™ and Taxotere [41]. The long $t_{1/2,\beta}$ of cRGD-MDTX and MDTX verified their better *in vivo* stability, owing to their disulfide cross-linking [30].

To study the biodistribution of the micellar DTX, Cy5-labeled cRGD-MDTX and MDTX were *i.v.* administered into the PC3 tumor-bearing mice, and the *in vivo* fluorescence images and *ex vivo* images of tumors and main organs were acquired and DTX was quantified. *In vivo* imaging showed that both micellar DTX formulations gathered swiftly in PC3 tumors at 1 h and were continuous to increase in 4 h (Fig. 3B). cRGD-MDTX remained a high tumor accumulation from 4 to 24 h while MDTX showed decrease of tumor accumulation. The *ex vivo* images and its semi-quantitative analysis demonstrated much higher tumor accumulation of cRGD-MDTX than MDTX at 24 h (**p, Fig. 3C, D). Moreover, HPLC quantifications revealed that DTX content of cRGD-MDTX group in tumors (8.3% ID/g) was *ca.* 3.1-fold that of MDTX group (Fig. 3E). Of note, both MDTX and cRGD-MDTX induced a low liver accumulation, in contrast to larger nanoparticles with similar surface properties [42] and small-sized nanoparticles without core-crosslinking [43]. This indicates that both particle size and core-crosslinking play a critical role in lessening liver accumulation. Moreover, cRGD-MDTX displayed slightly higher kidney accumulation, though not significant, than MDTX (Fig. 3D and E), which is likely due to expression of $\alpha_v\beta_3$ integrin on kidney podocytes [44]. Fig. 3F shows that cRGD-MDTX group had 1.8–3.8-fold enhancement on tumor-to-normal tissue (T/N) ratios over MDTX group. Interestingly, cRGD-MDTX enabled an extraordinary tumor-liver ratio of 2.8/1. T/N ratio is an important criterion for *in vivo* targetability [45], and high T/N ratio of cRGD-MDTX validated its tumor selectivity. Furthermore, tumor accumulation of cRGD-MDTX was enhanced by 2.9 folds from 3 h to 24 h post-injection (**p), in contrast to only slight increase for MDTX group (Fig. 3G). BIND-014 showed 1.5 times increase in tumor accumulation from 2 h to 12 h [46]. This greatly enhanced tumor accumulation for cRGD-MDTX was probably due to its high penetration and retention resulting from its small size and binding of

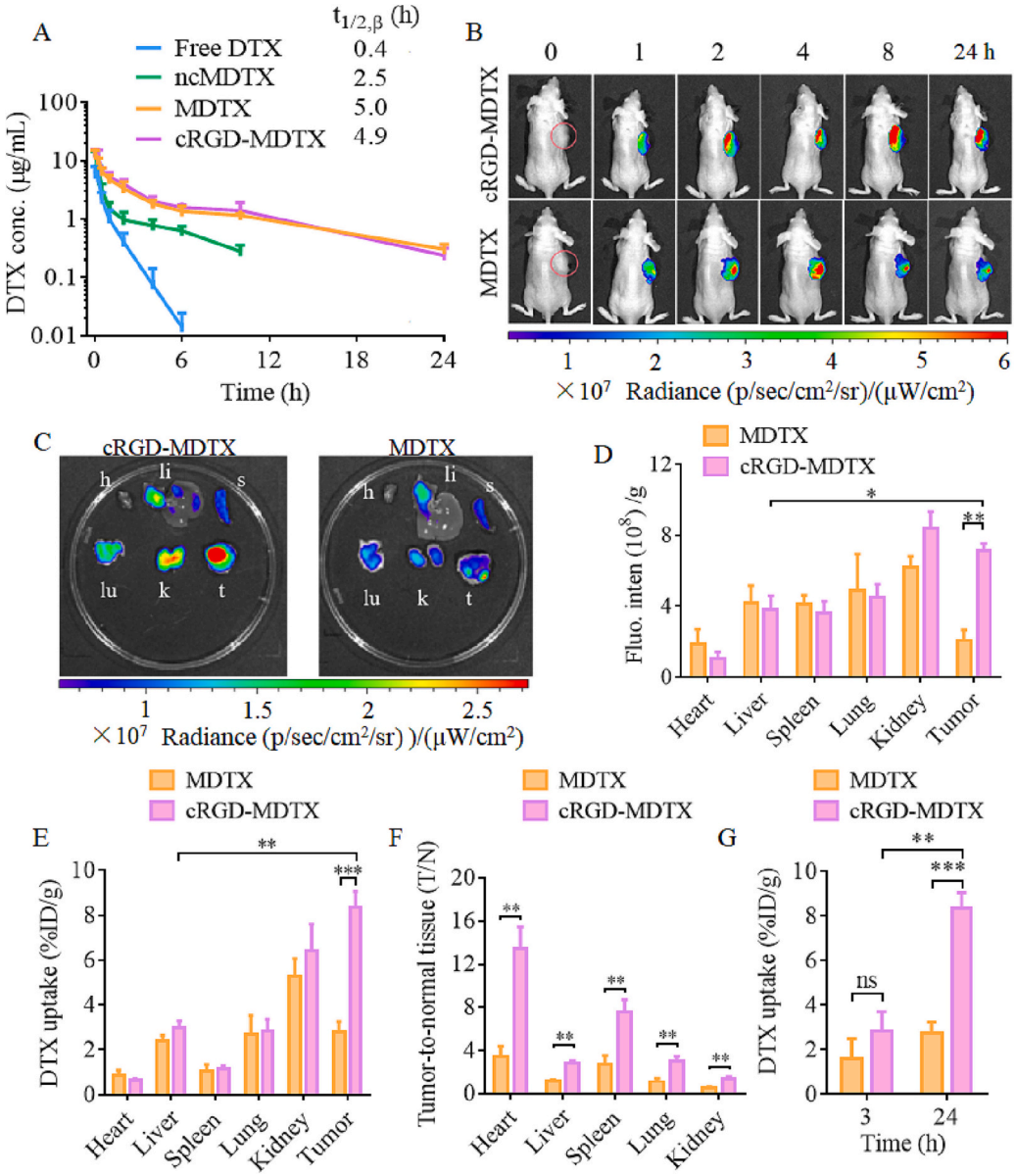

Fig. 3. The pharmacokinetics and biodistribution of micellar DTX in mice (DTX: 7.5 mg/kg). (A) Pharmacokinetics in healthy BALB/c mice. (B) *In vivo* fluorescence images of the mice bearing PC3 tumors post *i.v.* administration of Cy5-labeled MDTX or cRGD-MDTX. (C) *Ex vivo* images and (D) semi-quantification of fluorescence intensity of main organs and tumors at 24 h after administration (Cy5 dose: 0.2 μg/mouse). DTX biodistribution in major organs and tumors (E) and tumor to normal tissue (T/N) ratio (F) measured by HPLC. (G) Tumor accumulation of DTX at 3 h and 24 h. $^*p < 0.05$, $^{**}p < 0.01$, $^{***}p < 0.001$.

cRGD to tumor cells and vasculatures in PC3 tumors, in agreement with the *in vivo* imaging result (Fig. 3B). The liver accumulation is a major issue for nanomedicines. Typically, nanomedicines (size 30–200 nm) showed low tumor-liver ratios ranging from 0.15 to 1.2 [47–49] and rarely beyond 2.0 [50]. The present cRGD-MDTX may shine a light on how to mitigate liver accumulation and enhance tumor retention.

The distribution of Cy5-labeled micellar DTX inside tumors at 24 h post *i.v.* injection was examined using CLSM. The results showed strong and widespread Cy5 fluorescence for cRGD-MDTX at both tumor periphery region (Fig. 4A) and central area (Fig. 4B). In stark contrast, MDTX resided only in tumor periphery region and blood vessels. We have shown previously that cRGD-decorated larger-sized micellar drugs have poor tumor penetration [42]. The superior tumor deposition and penetration of cRGD-MDTX is attributable to a combined effect of small size, cRGD targeting and binding to $\alpha_v\beta_3$-overexpressing tumor cells and neovasculature in tumor tissues. It was reported that extracellular barriers like high interstitial fluid pressure and lowered transcapillary pressure gradients would prevent nanoparticles from penetration deep inside tumors [51–53]. In comparison with the sophisticated nanoparticles with charge-reversal (negative to positive) [13,14] and size changeable [15,16] properties explored for enhancing tumor penetration, the present cRGD-MDTX is biodegradable and facile to produce, representing a new strategy to promoting tumor distribution in solid tumors.

3.5. Therapeutic activity of cRGD-MDTX to mice bearing PC3 xenografts

cRGD density is a critical parameter for antitumor efficacy of active-targeting micellar drugs; however, its influence on tumor inhibition *in vivo* is seldom reported. Encouraged by the long circulation and high tumor penetration/deposition, we investigated therapeutic activity of cRGD-MDTX with varying cRGD densities in nude mice bearing PC3 tumors. The tumor growth curves demonstrated that all cRGD-MDTX were superior to MDTX, ncMDTX or free DTX ($^{***}p$) at DTX dose of 7.5 mg/kg *via i.v.* injection (Fig. 5A). Interestingly, 4% cRGD-MDTX significantly arrested tumor progression, much more profoundly than MDTX ($^{***}p$), 2% cRGD-MDTX ($^{**}p$), and 8% cRGD-MDTX ($^{*}p$), in agreement with *in vitro* MTT results, underscoring the critical role of cRGD density of nanodrugs in *in vivo* antitumor activity. Free DTX and ncMDTX had similar antitumor capability displaying limited tumor

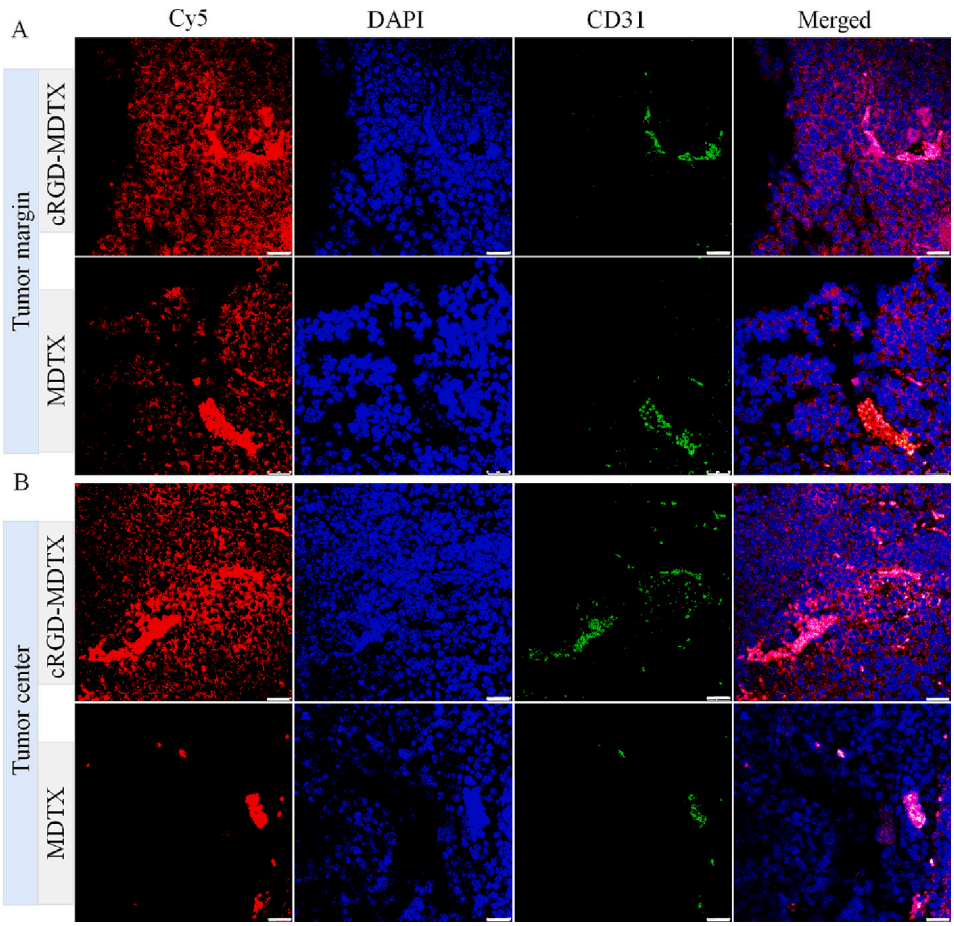

Fig. 4. CLSM images of Cy5-labeled cRGD-MDTX and MDTX at the margin (A) or in the center (B) of PC3 tumors at 24 h after *i.v.* injection. Red: micelles (Cy5), blue: nuclei (DAPI), and green: blood vessels (Alexa 488 labeled anti-CD31 antibody). Scale bar: 50 μm. (For interpretation of the references to colour in this figure legend, the reader is referred to the web version of this article.)

suppression compared to PBS group, while MDTX further reduced tumor volume (*p). Considering their similar size, drug loading content and surface property, the higher antitumor efficacy of MDTX than ncMDTX was primarily owing to the disulfide-crosslinks induced by DTC moieties in the micellar cores, which on one hand increase stability and prevent premature drug release and on the other hand trigger rapid DTX release inside tumor cells [45,54]. Meanwhile, all mice had constant body weight during treatment (Fig. 5B), confirming low side-effect of the formulations. The tumor inhibition rate (TIR) of 4% cRGD-MDTX on day 14 was *ca.* 94.6%, greatly higher than all other formulations (Fig. 5C). TUNEL staining images of tumor slices validated that 4% cRGD-MDTX induced enormous and widespread tumor apoptosis (Fig. 5D).

PC3 tumor was reportedly bone metastatic causing severe bone damage [55]. Here, the plasma concentrations of calcium ions and phosphate after treatment were determined. The results revealed indeed significantly higher ions of PBS mice than those of healthy mice (Fig. 5E). Of note, 4% cRGD-MDTX treated mice had drastically reduced plasma mineral concentrations and was comparable to healthy mice, verifying its protection from bone damage.

3.6. Therapeutic activity of cRGD-MDTX to mice bearing prostate PDX tumor

We further assessed the efficacy of cRGD-MDTX in prostate PDX model, which is the most relevant mouse model to clinics and frequently applied for drug development. The prostate PDX tumor model was established by subcutaneously inoculating tumor tissue of prostate cancer patient in NOD SCID mice. The PDX tumor showed high expression of α_v and β_3 integrins (Fig. S4). At tumor volume of *ca.* 100 mm^3, DTX formulations were *i.v.* administered on day 0, 3, 6 and 9 at DTX dose of 7.5 mg/kg. The results revealed that compared to fast tumor growth of PBS group, all four DTX formulations could inhibit tumor growth (Fig. 6A). MDTX showed significantly better inhibitory effect than ncMDTX and free DTX (**p). cRGD-MDTX was further superior to MDTX (***p) with clear shrinkage of tumors on day 30 and with slight gain in body weight (Fig. 6B).

3.7. Therapy of orthotopic A549 and SKOV3 xenograft bearing mice

DTX as broad-spectrum anticancer drug is clinically used for lung and ovarian cancers [56,57]. Western blot results showed that human non-small cell lung cancer A549 cells and ovarian cancer SKOV3 cells had high expression of α_v and β_3 (Fig. S4). Based on the excellent performance of cRGD-MDTX in prostate CDX and PDX models, we further investigated the antitumor activity in the mice bearing orthotopic A549-Luc or SKOV3-Luc tumor xenografts.

Orthotopic A549-Luc bearing mice were treated by *i.v.* injection of cRGD-MDTX (DTX: 7.5 mg/kg) at bioluminescence of 1×10^6 p/s/cm^2/sr and the bioluminescence was tracked in time. The *in vivo* imaging exposed that tumor bioluminescence of free DTX and PBS groups rapidly increased, while that of MDTX and cRGD-MDTX group drastically reduced (Fig. 7A). The semi-quantitative bioluminescence intensity results showed that the relative intensity (I_t/I_0) of PBS group rapidly increased to 16 on day 17, and the mice died before day 32 (Fig. 7B). The I_t/I_0 of free DTX, MDTX and cRGD-MDTX on day 32 was 21, 5 and 0.5 respectively, illustrating the pivotal role of the small micellar

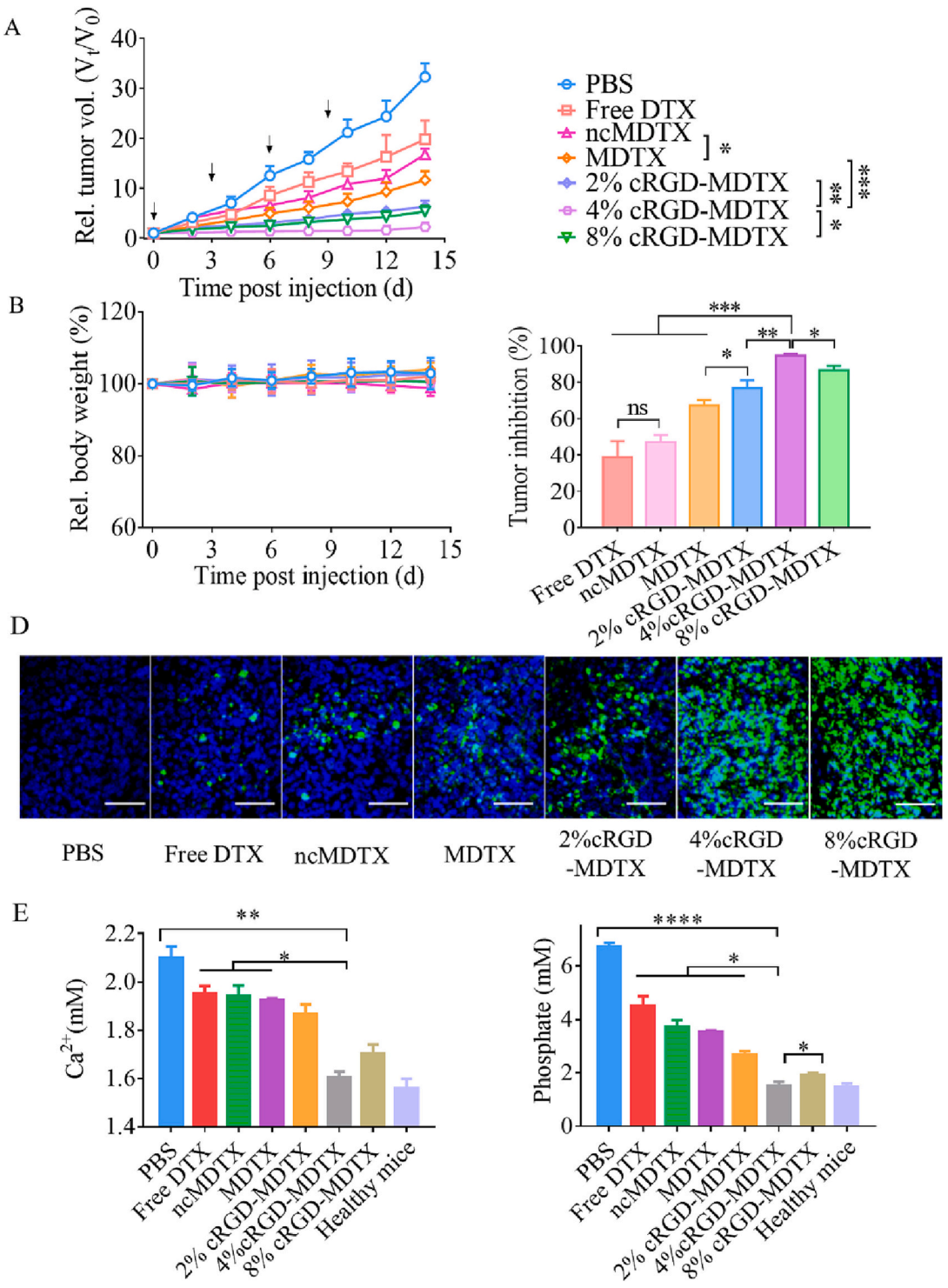

Fig. 5. Antitumor activity of cRGD-MDTX with various cRGD densities in PC3 tumor-bearing mice ($n = 5$) by *i.v.* administration on day 0, 3, 6, and 9 (DTX: 7.5 mg/kg). MDTX, ncMDTX, free DTX, and PBS were as controls. (A) Tumor growth curves. (B) Relative body weight of mice. (C) Tumor inhibition rates (TIR), (D) TUNEL images of tumor slices and (E) plasma concentrations of calcium ion and phosphate on day 14. Scale bar: 50 μm. *$p < 0.05$, **$p < 0.01$, ***$p < 0.001$.

nanocarrier and cRGD targeting on efficient antitumor activity. Importantly, cRGD-MDTX and MDTX groups did not show body weight loss, but PBS and free DTX groups lost body weight due to massive tumor invasion (Fig. 7C). Notably, Kaplan-Meier survival curves disclosed the significantly prolonged life spans of the mice treated with cRGD-MDTX (***p) and MDTX (**p) compared with PBS and free DTX groups (Fig. 7D). The median survival time (MST) of cRGD-MDTX (73 d) and MDTX (50 d) groups was 2.8- and 1.9-fold that PBS group (26 d), as compare to a 1.9-fold enhancement of MST by another DTX formulation cNGQ-PS-DTX [45], corroborating with the strong antitumor efficiency of cRGD-MDTX.

Toward the orthotopic SKOV3-Luc tumor model, the *i.v.* injection of cRGD-MDTX and MDTX obviously repressed tumor development (Fig. 8A). cRGD-MDTX treatment resulted in decreased bioluminescence thus tumor shrinkage, and had the lowest tumor bioluminescence among all groups (**p) (Fig. 8B) and constant body weights (Fig. 8C).

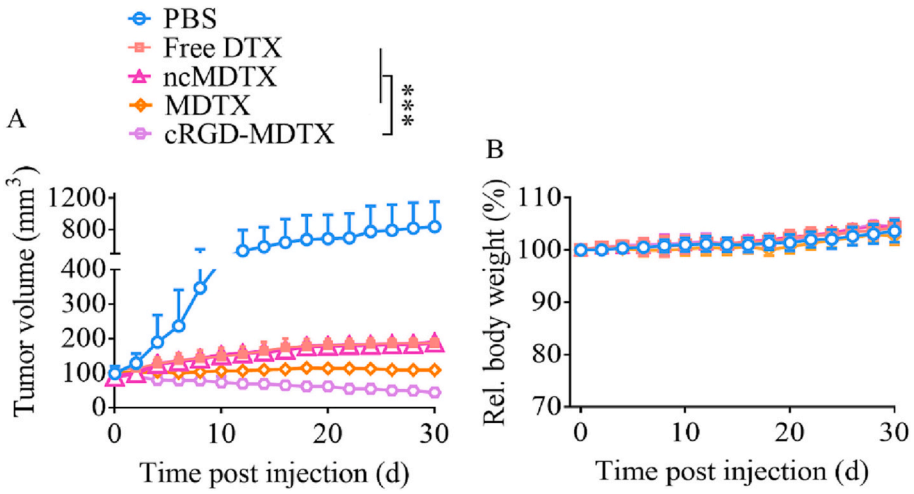

Fig. 6. Antitumor activity of cRGD-MDTX toward prostate tumor PDX model ($n = 5$) at *i.v.* administration on day 0, 3, 6, and 9 (DTX dose: 7.5 mg/kg). (A) Tumor volume. (B) Body weight relative to that on day 0. ***$p < 0.001$.

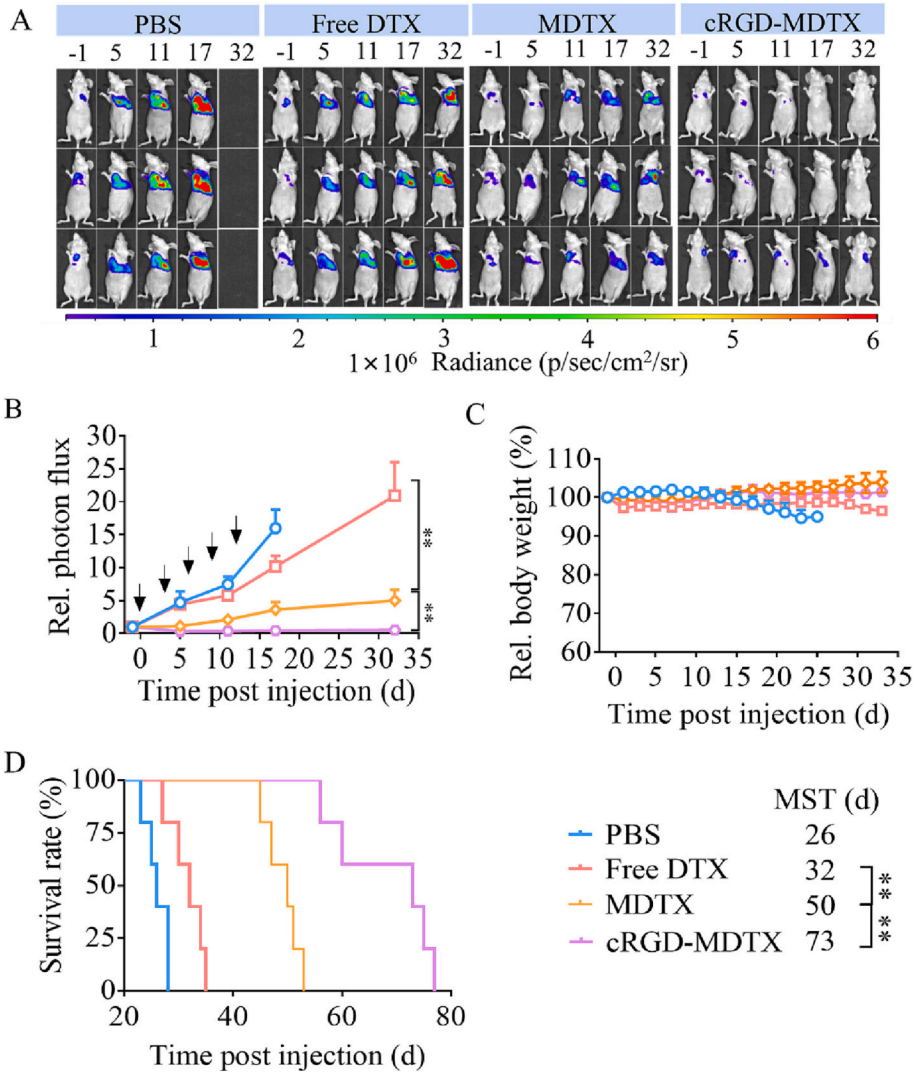

Fig. 7. Antitumor activity of cRGD-MDTX toward the mice bearing orthotopic A549-Luc tumors using MDTX, free DTX and PBS as controls ($n = 5$). The formulations were *i.v.* administered on day 0, 3, 6, 9 and 12 (DTX: 7.5 mg/kg). (A) *In vivo* bioluminescence imaging of mice. (B) Semi-quantitative bioluminescence intensity and (C) body weight relative to the values on day 0. (D) Kaplan-Meier survival curves. **$p < 0.01$, ***$p < 0.001$.

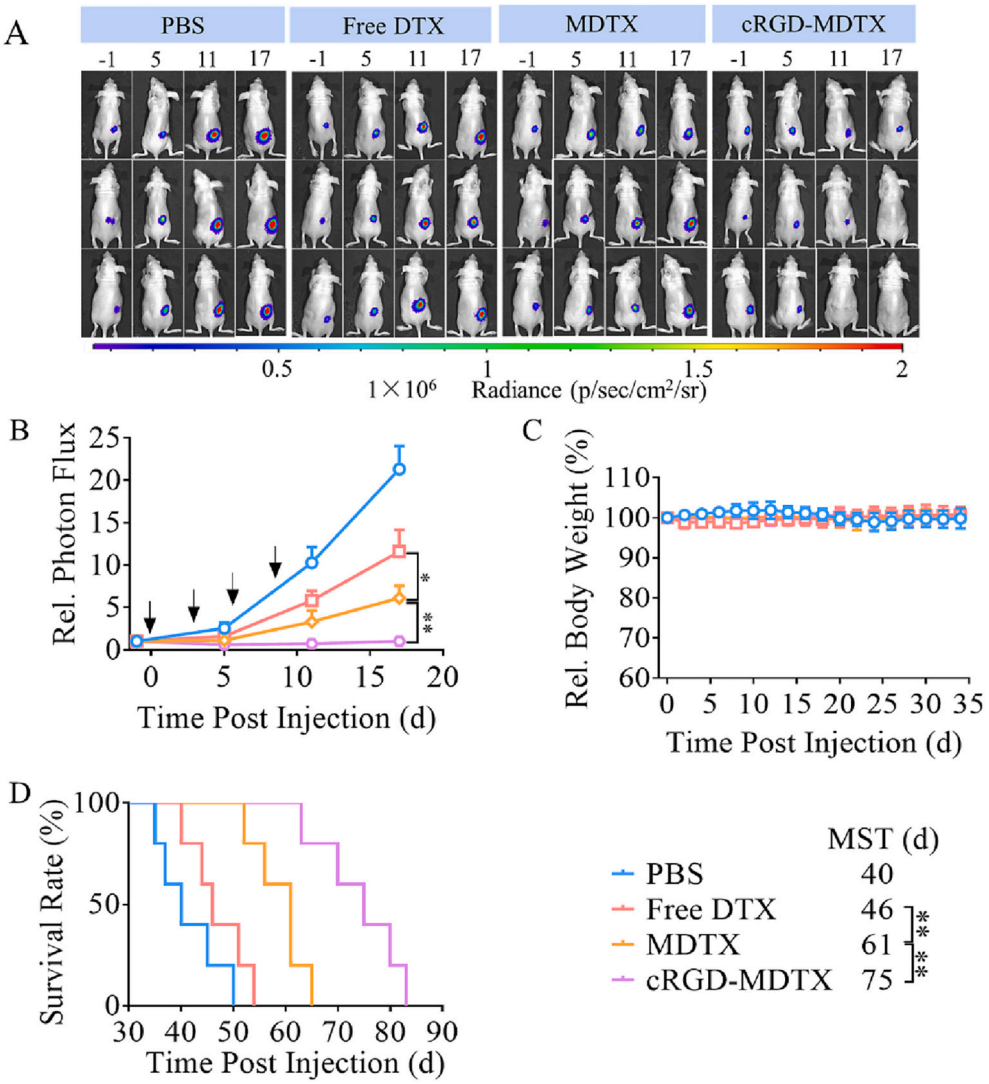

Fig. 8. Antitumor activity of cRGD-MDTX toward the mice bearing orthotopic SKOV3-Luc tumor using MDTX, free DTX and PBS as controls (n = 5). The formulations were *i.v.* administered on day 0, 3, 6, 9 and 12 (DTX: 7.5 mg/kg). (A) *In vivo* bioluminescence imaging of mice. (B) Semi-quantitative bioluminescence intensity and (C) body weight relative to the values on day 0. (D) Kaplan-Meier survival curves. $^{*}p < 0.05$, $^{**}p < 0.01$, $^{***}p < 0.001$.

cRGD-MDTX therapy greatly prolonged the MST to 75 days compared with MDTX (61 d, $^{**}p$) and free DTX (46 d, $^{****}p$) (Fig. 8 D). These results are extraordinary because ovarian cancer is known highly challenging to treat mainly due to the inaccessibility of drugs deep inside tumor tissues [58].

4. Conclusion

We have demonstrated that $\alpha_v\beta_3$ integrin-targeting 24 nm robust biodegradable micellar docetaxel (cRGD-MDTX) is able to mitigate liver deposition as well as target and penetrate deep into various types of solid tumors, resulting in superior chemotherapy of prostate CDX and PDX tumor models, and orthotopic lung and ovarian tumor models. cRGD-MDTX while simple is integrated with multiple intriguing features such as small size, high stability, evident tumor targeting and penetrating ability, and responsive drug release. cRGD-MDTX presents a unique and viable strategy to circumvent liver accumulation, rendering it particularly appealing for clinical translation.

CRediT authorship contribution statement

Wencheng Yan: Writing – original draft, Investigation, Formal analysis, Data curation. **Beibei Guo:** Validation, Investigation, Data curation. **Zhe Wang:** Investigation. **Jiangtao Yang:** Investigation, Data curation. **Zhiyuan Zhong:** Writing – review & editing, Supervision, Conceptualization. **Fenghua Meng:** Writing – review & editing, Supervision, Project administration, Methodology, Conceptualization.

Declaration of Competing Interest

None.

Data availability

Data will be made available on request.

Acknowledgement

This work is supported by research grants from the National Natural Science Foundation of China (NSFC 52033006, 52233007).

Appendix A. Supplementary data

Supplementary data to this article can be found online at https://doi.

org/10.1016/j.jconrel.2023.06.032.

References

[1] R. van der Meel, E. Sulheim, Y. Shi, F. Kiessling, W.J.M. Mulder, T. Lammers, Smart cancer nanomedicine, Nat. Nanotechnol. 14 (2019) 1007–1017, https://doi.org/10.1038/s41565-019-0567-y.

[2] S.N. Bhatia, X. Chen, M.A. Dobrovolskaia, T. Lammers, Cancer nanomedicine, Nat. Rev. Cancer 22 (2022) 550–556, https://doi.org/10.1038/s41568-022-00496-9.

[3] Y.N. Zhang, W. Poon, A.J. Tavares, I.D. McGilvray, W.C.W. Chan, Nanoparticle-liver interactions: cellular uptake and hepatobiliary elimination, J. Control. Release 240 (2016) 332–348, https://doi.org/10.1016/j.jconrel.2016.01.020.

[4] M.J. Ernsting, M. Murakami, A. Roy, S.D. Li, Factors controlling the pharmacokinetics, biodistribution and intratumoral penetration of nanoparticles, J. Control. Release 172 (2013) 782–794, https://doi.org/10.1016/j.jconrel.2013.09.013.

[5] B. Yameen, W.I. Choi, C. Vilos, A. Swami, J. Shi, O.C. Farokhzad, Insight into nanoparticle cellular uptake and intracellular targeting, J. Control. Release 190 (2014) 485–499, https://doi.org/10.1016/j.jconrel.2014.06.038.

[6] W. Poon, Y.N. Zhang, B. Ouyang, B.R. Kingston, J.L.Y. Wu, S. Wilhelm, W.C. W. Chan, Elimination pathways of nanoparticles, ACS Nano 13 (2019) 5785–5798, https://doi.org/10.1021/acsnano.9b01383.

[7] C.D. Walkey, J.B. Olsen, H. Guo, A. Emili, W.C.W. Chan, Nanoparticle size and surface chemistry determine serum protein adsorption and macrophage uptake, J. Am. Chem. Soc. 134 (2012) 2139–2147, https://doi.org/10.1021/ja2084338.

[8] N. Dammes, M. Goldsmith, S. Ramishetti, J.L.J. Dearling, N. Veiga, A.B. Packard, D. Peer, Conformation-sensitive targeting of lipid nanoparticles for RNA therapeutics, Nat. Nanotechnol. 16 (2021) 1030–1038, https://doi.org/10.1038/s41565-021-00928-x.

[9] M.O. Durymanov, A.A. Rosenkranz, A.S. Sobolev, Current approaches for improving intratumoral accumulation and distribution of nanomedicines, Theranostics. 5 (2015) 1007–1020, https://doi.org/10.7150/thno.11742.

[10] Q. Hu, C.J.F. Rijcken, E. van Gaal, P. Brundel, H. Kostkova, T. Etrych, B. Weber, M. Barz, F. Kiessling, J. Prakash, G. Storm, W.E. Hennink, T. Lammers, Tailoring the physicochemical properties of core-crosslinked polymeric micelles for pharmaceutical applications, J. Control. Release 244 (2016) 314–325, https://doi.org/10.1016/j.jconrel.2016.07.012.

[11] L. Tang, X. Yang, Q. Yin, K. Cai, H. Wang, I. Chaudhury, C. Yao, Q. Zhou, M. Kwon, J.A. Hartman, I.T. Dobrucki, L.W. Dobrucki, L.B. Borst, S. Lezmi, W.G. Helferich, A. L. Ferguson, T.M. Fan, J. Cheng, Investigating the optimal size of anticancer nanomedicine, Proc. Natl. Acad. Sci. U. S. A. 111 (2014) 15344–15349, https://doi.org/10.1073/pnas.1411499111.

[12] B. Louage, O. De Wever, W.E. Hennink, B.G. De Geest, Developments and future clinical outlook of taxane nanomedicines, J. Control. Release 253 (2017) 137–152, https://doi.org/10.1016/j.jconrel.2017.03.027.

[13] J. Chen, J. Ding, Y. Wang, J. Cheng, S. Ji, X. Zhuang, X. Chen, Sequentially responsive shell-stacked nanoparticles for deep penetration into solid tumors, Adv. Mater. 29 (2017) 1701170, https://doi.org/10.1002/adma.201701170.

[14] D. Li, C.F. van Nostrum, E. Mastrobattista, T. Vermonden, W.E. Hennink, Nanogels for intracellular delivery of biotherapeutics, J. Control. Release 259 (2017) 16–28, https://doi.org/10.1016/j.jconrel.2016.12.020.

[15] R. Tong, H.H. Chiang, D.S. Kohane, Photoswitchable nanoparticles for in vivo cancer chemotherapy, Proc. Natl. Acad. Sci. U. S. A. 110 (2013) 19048–19053, https://doi.org/10.1073/pnas.1315336110.

[16] W. Yu, C. Hu, H. Gao, Intelligent size-changeable nanoparticles for enhanced tumor accumulation and deep penetration, ACS Appl. Bio. Mater. 3 (2020) 5455–5462, https://doi.org/10.1021/acsabm.0c00917.

[17] W. Gu, F. Meng, R. Haag, Z. Zhong, Actively targeted nanomedicines for precision cancer therapy: concept, construction, challenges and clinical translation, J. Control. Release 329 (2021) 676–695, https://doi.org/10.1016/j.jconrel.2020.10.003.

[18] B. Guo, J. Wei, J. Wang, Y. Sun, J. Yuan, Z. Zhong, F. Meng, CD44-targeting hydrophobic phosphorylated gemcitabine prodrug nanotherapeutics augment lung cancer therapy, Acta Biomater. 145 (2022) 200–209, https://doi.org/10.1016/j.actbio.2022.04.016.

[19] R. Han, Q. Liu, Y. Lu, J. Peng, M. Pan, G. Wang, W. Chen, Y. Xiao, C. Yang, Z. Qian, Tumor microenvironment-responsive Ag_2S-PAsp(DOX)-cRGD nanoparticles-mediated photochemotherapy enhances the immune response to tumor therapy, Biomaterials. 281 (2022), 121328, https://doi.org/10.1016/j.biomaterials.2021.121328.

[20] R.J. Slack, S.J.F. Macdonald, J.A. Roper, R.G. Jenkins, R.J.D. Hatley, Emerging therapeutic opportunities for integrin inhibitors, Nat. Rev. Drug Discov. 21 (2022) 60–78, https://doi.org/10.1038/s41573-021-00284-4.

[21] A. Sheikh, S. Md, P. Kesharwani, RGD engineered dendrimer nanotherapeutic as an emerging targeted approach in cancer therapy, J. Control. Release 340 (2021) 221–242, https://doi.org/10.1016/j.jconrel.2021.10.028.

[22] M.M. Gomari, S. Abkhiz, T.G. Pour, E. Lotfi, N. Rostami, F.N. Monfared, B. Ghobari, M. Mosavi, B. Alipour, N.V. Dokholyan, Peptidomimetics in cancer targeting, Mol. Med. 28 (2022) 146, https://doi.org/10.1186/s10020-022-00577-3.

[23] K.S. de Valk, M.M. Deken, H.J.M. Handgraaf, S.S. Bhairosingh, O.D. Bijlstra, M. J. van Esdonk, A.G.T.T. van Scheltinga, A.R.P.M. Valentijn, T.L. March, J. Vuijk, K. C.M.J. Peeters, F.A. Holman, D.E. Hilling, J.S.D. Mieog, J.V. Frangioni, J. Burggraaf, A.L. Vahrmeijer, First-in-human assessment of cRGD-ZW800-1, a zwitterionic, integrin-targeted, near-infrared fluorescent peptide in colon carcinoma, Clin. Cancer Res. 26 (2020) 3990–3998, https://doi.org/10.1158/1078-0432.CCR-19-4156.

[24] Y. Miura, T. Takenaka, K. Toh, S. Wu, H. Nishihara, M.R. Kano, Y. Ino, T. Nomoto, Y. Matsumoto, H. Koyama, H. Cabral, N. Nishiyama, K. Kataoka, Cyclic RGD-linked polymeric micelles for targeted delivery of platinum anticancer drugs to glioblastoma through the blood-brain tumor barrier, ACS Nano 7 (2013) 8583–8592, https://doi.org/10.1021/nn402662d.

[25] F. Zhang, Q. Ni, O. Jacobson, S. Cheng, A. Liao, Z. Wang, Z. He, G. Yu, J. Song, Y. Ma, G. Niu, L. Zhang, G. Zhu, X. Chen, Polymeric nanoparticles with a glutathione-sensitive heterodimeric multifunctional prodrug for in vivo drug monitoring and synergistic cancer therapy, Angew. Chem. Int. Ed. 57 (2018) 7066–7070, https://doi.org/10.1002/anie.201801984.

[26] Y. Zou, J. Wei, Y. Xia, F. Meng, J. Yuan, Z. Zhong, Targeted chemotherapy for subcutaneous and orthotopic non-small cell lung tumors with cyclic RGD-functionalized and disulfide-crosslinked polymersomal doxorubicin, Signal Transduct. Target. Ther. 3 (2018) 32, https://doi.org/10.1038/s41392-018-0032-7.

[27] Y. Zou, M. Zheng, W. Yang, F. Meng, K. Miyata, H.J. Kim, K. Kataoka, Z. Zhong, Virus-mimicking chimaeric polymersomes boost targeted cancer siRNA therapy in vivo, Adv. Mater. 29 (2017) 1703285, https://doi.org/10.1002/adma.201703285.

[28] S. Sharma, V.R. Kotamraju, T. Mölder, A. Tobi, T. Teesalu, E. Ruoslahti, Tumor-penetrating nanosystem strongly suppresses breast tumor growth, Nano Lett. 17 (2017) 1356–1364, https://doi.org/10.1021/acs.nanolett.6b03815.

[29] R. Ridolfo, B.C. Ede, P. Diamanti, P.B. White, A.W. Perriman, J.C.M. van Hest, A. Blair, D.S. Williams, Biodegradable, drug-loaded nanovectors via direct hydration as a new platform for cancer therapeutics, Small. 14 (2018) 1703774, https://doi.org/10.1002/smll.201703774.

[30] X. Qiu, Y. Qu, B. Guo, H. Zheng, F. Meng, Z. Zhong, Micellar paclitaxel boosts ICD and chemo-immunotherapy of metastatic triple negative breast cancer, J. Control. Release 341 (2022) 498–510, https://doi.org/10.1016/j.jconrel.2021.12.002.

[31] L. Tan, J. Peng, Q. Zhao, L. Zhang, X. Tang, L. Chen, M. Lei, Z. Qian, A novel MPEG-PDLLA-PLL copolymer for docetaxel delivery in breast cancer therapy, Theranostics. 7 (2017) 2652–2672, https://doi.org/10.7150/thno.19680.

[32] W. Yu, R. Liu, Y. Zhou, H. Gao, Size-tunable strategies for a tumor targeted drug delivery system, ACS Cent. Sci. 6 (2020) 100–116, https://doi.org/10.1021/acscentsci.9b01139.

[33] J. Ding, J. Chen, L. Gao, Z. Jiang, Y. Zhang, M. Li, Q. Xiao, S.S. Lee, X. Chen, Engineered nanomedicines with enhanced tumor penetration, Nano Today 29 (2019), 100800, https://doi.org/10.1016/j.nantod.2019.100800.

[34] J. Nai, J. Zhang, J. Li, H. Li, Y. Yang, M. Yang, Y. Wang, W. Gong, Z. Li, L. Li, C. Gao, Macrophage membrane- and cRGD-functionalized thermosensitive liposomes combined with CPP to realize precise siRNA delivery into tumor cells, Mol. Ther. Nucl. Acids 27 (2022) 349–362, https://doi.org/10.1016/j.omtn.2021.12.016.

[35] C.J. Avraamides, B. Garmy-Susini, J.A. Varner, Integrins in angiogenesis and lymphangiogenesis, Nat. Rev. Cancer 8 (2008) 604–617, https://doi.org/10.1038/nrc2353.

[36] A.P. Sangnier, S. Preveral, A. Curcio, A.K.A. Silva, C.T. Lefevre, D. Pignol, Y. Lalatonne, C. Wilhelm, Targeted thermal therapy with genetically engineered magnetite magnetosomes@RGD: Photothermia is far more efficient than magnetic hyperthermia, J. Control. Release 279 (2018) 271–281, https://doi.org/10.1016/j.jconrel.2018.04.036.

[37] J. Dai, Y. Li, Z. Long, R. Jiang, Z. Zhuang, Z. Wang, Z. Zhao, X. Lou, F. Xia, B. Z. Tang, Efficient near-infrared photosensitizer with aggregation-induced emission for imaging-guided photodynamic therapy in multiple xenograft tumor models, ACS Nano 14 (2020) 854–866, https://doi.org/10.1021/acsnano.9b07972.

[38] J. Wei, Y. Xia, F. Meng, D. Ni, X. Qiu, Z. Zhong, Small, smart, and LDLR-specific micelles augment sorafenib therapy of glioblastoma, Biomacromolecules. 22 (2021) 4814–4822, https://doi.org/10.1021/acs.biomac.1c01103.

[39] D.R. Elias, A. Poloukhtine, V. Popik, A. Tsourkas, Effect of ligand density, receptor density, and nanoparticle size on cell targeting, Nanomed. Nanotechnol. 9 (2013) 194–201, https://doi.org/10.1016/j.nano.2012.05.015.

[40] J. Kim, J. Lee, J. Lee, H. Keum, Y. Kim, Y. Kim, B. Yu, S.Y. Lee, J. Tanaka, S. Jon, M. C. Choi, Tubulin-based nanotubes as delivery platform for microtubule-targeting agents, Adv. Mater. 32 (2020) 2002902, https://doi.org/10.1002/adma.202002902.

[41] S.W. Lee, M.H. Yun, S.W. Jeong, C.H. In, J.Y. Kim, M.H. Seo, C.M. Pai, S.O. Kim, Development of docetaxel-loaded intravenous formulation, Nanoxel-PMTM using polymer-based delivery system, J. Control. Release 155 (2011) 262–271, https://doi.org/10.1016/j.jconrel.2011.06.012.

[42] Y. Zhu, J. Zhang, F. Meng, C. Deng, R. Cheng, J. Feijen, Z. Zhong, cRGD/TAT dual-ligand reversibly cross-linked micelles loaded with docetaxel penetrate deeply into tumor tissue and show high antitumor efficacy in vivo, ACS Appl. Mater. Interfaces 9 (2017) 35651–35663, https://doi.org/10.1021/acsami.7b12439.

[43] P. Zhong, M. Qiu, J. Zhang, H. Sun, R. Cheng, C. Deng, F. Meng, Z. Zhong, cRGD-installed docetaxel-loaded mertansine prodrug micelles: redox-triggered ratiometric dual drug release and targeted synergistic treatment of B16F10 melanoma, Nanotechnol. 28 (2017), 295103, https://doi.org/10.1088/1361-6528/aa76cc.

[44] Z. Hafdi, P. Lesavre, M. Nejjari, L. Halbwachs-Mecarelli, D. Droz, L.H. Noel, Distribution of alphavbeta3, alphavbeta5 integrins and the integrin associated protein–IAP (CD47) in human glomerular diseases, Cell Commun. Adhes. 7 (2000) 441–451, https://doi.org/10.3109/15419060009040302.

[45] Y. Zou, Y. Sun, B. Guo, Y. Wei, Y. Xia, Z. Huangfu, F. Meng, J.C.M. van Hest, J. Yuan, Z. Zhong, Alpha(3)beta(1) integrin-targeting polymersomal docetaxel as an advanced nanotherapeutic for nonsmall cell lung cancer treatment, ACS Appl.

Mater. Interfaces 12 (2020) 14905–14913, https://doi.org/10.1021/acsami.0c01069.
[46] J. Hrkach, D. Von Hoff, M.M. Ali, E. Andrianova, J. Auer, T. Campbell, D.D. Witt, M. Figa, M. Figueiredo, A. Horhota, S. Low, K. McDonnell, E. Peeke, B. Retnarajan, A. Sabnis, E. Schnipper, J.J. Song, Y.H. Song, J. Summa, D. Tompsett, G. Troiano, T. Van, G. Hoven, J. Wright, P. LoRusso, P.W. Kantoff, N.H. Bander, C. Sweeney, O. C. Farokhzad, R. Langer, S. Zale, Preclinical development and clinical translation of a PSMA-targeted docetaxel nanoparticle with a differentiated pharmacological profile, Sci. Transl. Med. 4 (2012) 128ra139, https://doi.org/10.1126/scitranslmed.3003651.
[47] H. Fang, X. Zhao, X. Gu, H. Sun, R. Cheng, Z. Zhong, C. Deng, CD44-targeted multifunctional nanomedicines based on a single-component hyaluronic acid conjugate with all-natural precursors: construction and treatment of metastatic breast tumors in vivo, Biomacromolecules. 21 (2020) 104–113, https://doi.org/10.1021/acs.biomac.9b01012.
[48] P.R. Neumann, F. Erdmann, J. Holthof, G. Hadrich, M. Green, J. Rao, L.A. Dailey, Different PEG-PLGA matrices influence in vivo optical/photoacoustic imaging performance and biodistribution of NIR-emitting pi-conjugated polymer contrast agents, Adv. Healthc. Mater. 10 (2021) 2001089, https://doi.org/10.1002/adhm.202001089.
[49] J. Liu, F. Hu, M. Wu, L. Tian, F. Gong, X. Zhong, M. Chen, Z. Liu, B. Liu, Bioorthogonal coordination polymer nanoparticles with aggregation-induced emission for deep tumor-penetrating radio- and radiodynamic therapy, Adv. Mater. 33 (2021) 2007888, https://doi.org/10.1002/adma.202007888.
[50] I. Biancacci, Q. Sun, D. Mockel, F. Gremse, S. Rosenhain, F. Kiessling, M. Bartneck, Q. Hu, M. Thewissen, G. Storm, W.E. Hennink, Y. Shi, C.J.F. Rijcken, T. Lammers, A.M. Sofias, Optical imaging of the whole-body to cellular biodistribution of clinical-stage PEG-b-pHPMA-based core-crosslinked polymeric micelles, J. Control. Release 328 (2020) 805–816, https://doi.org/10.1016/j.jconrel.2020.09.046.
[51] Q. Sun, Z. Zhou, N. Qiu, Y. Shen, Rational design of cancer nanomedicine: nanoproperty integration and synchronization, Adv. Mater. 29 (2017) 1606628, https://doi.org/10.1002/adma.201606628.
[52] C.H. Heldin, K. Rubin, K. Pietras, A. Ostman, High interstitial fluid pressure-an obstacle in cancer therapy, Nat. Rev. Cancer 4 (2004) 806–813, https://doi.org/10.1038/nrc1456.
[53] J. Wang, Q. Ni, Y. Wang, Y. Zhang, H. He, D. Gao, X. Ma, X.J. Liang, Nanoscale drug delivery systems for controllable drug behaviors by multi-stage barrier penetration, J. Control. Release 331 (2021) 282–295, https://doi.org/10.1016/j.jconrel.2020.08.045.
[54] F. Lin, D. Wen, X. Wang, R.I. Mahato, Dual responsive micelles capable of modulating miRNA-34a to combat taxane resistance in prostate cancer, Biomaterials. 192 (2019) 95–108, https://doi.org/10.1016/j.biomaterials.2018.10.036.
[55] M. Landgraf, C.A. Lahr, A. Sanchez-Herrero, C. Meinert, A. Shokoohmand, P. M. Pollock, D.W. Hutmacher, A. Shafiee, J.A. McGovern, Humanized bone facilitates prostate cancer metastasis and recapitulates therapeutic effects of zoledronic acid in vivo, Bone Res. 7 (2019) 31, https://doi.org/10.1038/s41413-019-0072-9.
[56] Y. Mao, M. Hu, G. Yang, E. Gao, W. Chen, Current status of castration-resistant prostate cancer drug therapy, Int. J. Surg. Oncol. 6 (2021) 41–49, https://doi.org/10.29337/ijsonco.126.
[57] K. Ahmad, E.J. Lee, S. Shaikh, A. Kumar, K.M. Rao, S.Y. Park, J.O. Jin, S.S. Han, I. Choi, Targeting integrins for cancer management using nanotherapeutic approaches: recent advances and challenges, Semin. Cancer Biol. 69 (2021) 325–336, https://doi.org/10.1016/j.semcancer.2019.08.030.
[58] Z. Wang, F. Meng, Z. Zhong, Emerging targeted drug delivery strategies toward ovarian cancer, Adv. Drug Deliv. Rev. 178 (2021), 113969, https://doi.org/10.1016/j.addr.2021.113969.